# Substructures in the core of Abell 2319

Ichinohe, Y.; Simionescu, A.; Werner, N.; Markevitch, M.; Wang, Q.H.S.

MNRAS 000, 1–10 (2020) Preprint 22 November 2021 Compiled using MNRAS LATEX style file v3.0

# Substructures in the core of Abell 2319

Y. Ichinohe,[1]★ A. Simionescu,[2,3,4] N. Werner,[5,6] M. Markevitch,[7] and Q. H. S. Wang[8]
[1]Department of Physics, Rikkyo University, 3-34-1 Nishi-Ikebukuro, Toshima-ku, Tokyo 171-8501, Japan
[2]SRON Netherlands Institute for Space Research, Sorbonnelaan 2, NL-3584 CA Utrecht, the Netherlands
[3]Leiden Observatory, Leiden University, PO Box 9513, 2300 RA Leiden, The Netherlands
[4]Kavli Institute for the Physics and Mathematics of the Universe (WPI), The University of Tokyo, Kashiwa, Chiba 277-8583, Japan
[5]Department of Theoretical Physics and Astrophysics, Faculty of Science, Masaryk University, Kotlarská 2, Brno CZ-611 37, Czech Republic
[6]School of Science, Hiroshima University, 1-3-1 Kagamiyama, Higashi-Hiroshima 739-8526, Japan
[7]NASA/Goddard Space Flight Center, Greenbelt, MD 20771, USA
[8]Department of Physics and Astronomy, University of Utah, 115 South 1400 East, Salt Lake City, UT 84112, USA



22 November 2021

**ABSTRACT**

We analysed the deep archival *Chandra* observations of the high-temperature galaxy cluster Abell 2319 to investigate the prominent cold front in its core. The main sharp arc of the front shows wiggles, or variations of the radius of the density jump along the arc. At the southern end of the arc is a feature that resembles a Kelvin-Helmholtz (KH) eddy, beyond which the sharp front dissolves. These features suggest that KH instabilities develop at the front. Under this assumption, we can place an upper limit on the ICM viscosity that is several times below the isotropic Spitzer value. Other features include a split of the cold front at its northern edge, which may be another KH eddy. There is a small pocket of hot, less-dense gas inside the cold front, which may indicate a 'hole' in the front's magnetic insulation layer that lets the heat from the outer gas to penetrate inside the front. Finally, a large concave brightness feature southwest of the cluster core can be caused by the gasdynamic instabilities. We speculate that it can also be an inner boundary of a giant AGN bubble, similar to that in Ophiuchus. If the latter interpretation is supported by better radio data, this could be a remnant of another extremely powerful AGN outburst.

**Key words:** galaxies: clusters: individual: Abell 2319 – galaxies: clusters: intracluster medium – X-rays: galaxies: clusters

## 1 INTRODUCTION

Since its launch in 1999, *Chandra* has revealed a large number of fine X-ray morphological substructures in the intracluster medium (ICM), the most dominant baryonic component in clusters of galaxies. ICM substructure is a consequence of various cluster activities such as interactions with the central active galactic nucleus (AGN), mergers with other clusters or groups, and motions of its member galaxies. In the formation of these substructures, the ICM follows the physical laws, and thus, ICM substructures reflect the underlying physical properties of the ICM such as magnetic field strengths, viscosity and heat conductivity, little of which is well understood so far.

Among the substructures discovered by *Chandra* are cold fronts, the interface between two gas phases in pressure equilibrium: cooler and denser gas, and the hot and thin ambient medium (see Markevitch & Vikhlinin 2007, for a review). The first cold fronts were found in Abell 2142 (Markevitch et al. 2000) and in Abell 3667 (Vikhlinin et al. 2001a,b). Since then, cold fronts have been observed in a variety of locations and environmental setups (e.g., Fabian et al. 2006; Machacek et al. 2006; Owers et al. 2009; Ghizzardi et al. 2010) and it has been revealed that they are actually more common than shock fronts.

Cold fronts are roughly classified into two categories. Cold fronts in the first category appear when a cool gas blob from another subcluster is moving through the hot ambient medium, and are referred to as merger cold fronts (e.g., Vikhlinin et al. 2001a,b; Wang et al. 2016; Su et al. 2017). The second category occurs when a galaxy cluster undergoes a minor merger with non-zero impact parameter, so that the ICM gains angular momentum and starts swirling subsonically inside the cluster's gravitational potential (gas sloshing; Ascasibar & Markevitch 2006; Ichinohe et al. 2015; Ueda et al. 2020). As a result, a characteristic spiral-shaped morphological feature appears in the X-ray image, with cold fronts located along the edge of the spiral and referred to as sloshing cold fronts (e.g., Markevitch et al. 2000; Roediger et al. 2013b).

One of the important properties of cold fronts is their remarkable sharpness. The thickness of the interface is not resolved even by *Chandra*'s angular resolution (Vikhlinin et al. 2001a,b). This indicates that diffusive processes are suppressed at the interface because of, e.g., the small gyroradii of the electrons resulting from the draping magnetic fields.

Initially, cold fronts were regarded as single distinct substructures. However, recently, substructures of such substructures, i.e., substructures associated with cold fronts have been attracting attention as the tool to infer the underlying ICM microphysics. For example, Werner et al. (2016a) reported the presence of quasi-linear features underneath the cold front in the Virgo cluster. By comparison with a tailored numerical simulation, they suggested that these features are due to the amplification of magnetic fields by gas sloshing. Similar narrow structures of surface brightness were also found in several

★ E-mail: ichinohe@rikkyo.ac.jp

other systems; possible plasma depletion layers seen in projection (*X-ray channels*) were found in Abell 520 and Abell 2142 (Wang et al. 2016; Wang & Markevitch 2018); Ichinohe et al. (2019) found alternating bright and faint regions (*feathers*) in the Perseus cluster and estimated the amplified magnetic field strength at $\sim$30 $\mu$G. Several simulation studies have also been performed for magnetized gas sloshing (ZuHone et al. 2011, 2015).

Besides the features *inside* cold fronts, features *on* the cold front have also been extensively studied. As gas shear is inevitable at the cold front interface, fluid instabilities can develop under certain conditions. Su et al. (2017) found a multiple-edge profile of the merger cold front in the NGC 1404 galaxy, which is likely attributed to Kelvin-Helmholtz instabilities (KHI) seen in projection (Roediger et al. 2013b). Similar multiple-edge surface brightness profiles were also found in Abell 3667 (Ichinohe et al. 2017) and in the Perseus cluster (Ichinohe et al. 2019). At small scales, the existence of KHI whose size of less than kpc is indicated in the core of the Ophiuchus cluster (Werner et al. 2016b), while at large scales, Walker et al. (2017) suggested that a KHI roll with a size of $\sim$50 kpc exists east of the core of the Perseus cluster.

Abell 2319 ($z \sim 0.056$; 1 arcsec $\sim$1.08 kpc) is the fifth brightest cluster in the X-ray sky (Edge et al. 1990). The early *Chandra* observations made by O'Hara et al. (2004) and Govoni et al. (2004) revealed its high temperature and the existence of the sharp cold front extending for $\sim$300 kpc to the southeast of the brightness peak of the system. Both of these features as well as its giant radio halo (Harris & Miley 1978; Feretti et al. 1997; Govoni et al. 2001; Farnsworth et al. 2013) indicate a major merger activity ongoing in this system, and there has been a wide range of studies in this context (Markevitch 1996; Million & Allen 2009; Sugawara et al. 2009; Yan et al. 2014; Storm et al. 2015). Abell 2319 is the most significant Sunyaev-Zel'dovich effect (SZ; Sunyaev & Zeldovich 1972) detection in the *Planck* 2nd Sunyaev-Zeldovich Source Catalog (Planck Collaboration et al. 2016) and detailed studies using *XMM-Newton* aiming at probing the outskirts of the cluster have been performed (Eckert et al. 2014; Ghirardini et al. 2018; Hurier et al. 2019).

There have been several studies in terms of the cold front itself; Ghizzardi et al. (2010) reconfirmed the existence of the front using *XMM-Newton* data; ZuHone et al. (2013) used the *Chandra* image for visual comparison with numerical simulation images; Walker et al. (2016) used the *Chandra* image to demonstrate the Gaussian gradient magnitude filtering method. However, despite its prominence, there seem to have been no observational quantitative estimations of ICM microphysics performed using this cold front so far.

In this paper, we investigate in detail the currently available $\sim$90 ks archival *Chandra* data of Abell 2319 to explore the phenomena associated with this remarkable cold front and the physical implications derived from it. The high temperature and moderate density environment around the cold front in Abell 2319 is advantageous compared to other brightest clusters in that the Coulomb mean free paths of the electrons are much longer in this system.

We adopted the abundance table of proto-solar metal from Lodders & Palme (2009) for this paper. Unless otherwise noted, the error bars correspond to 68% confidence level for one parameter. Throughout this paper, we assume the standard $\Lambda$CDM cosmological model with the parameters of $(\Omega_m, \Omega_\Lambda, H_0) = (0.3, 0.7, 70\ \mathrm{km/s/Mpc})$.

**Table 1.** Summary of the observations used in this paper. The net exposure time is after the data screening.

| Obs ID | Date | Net exposure time (ks) |
|---|---|---|
| 3231 | 2002-03-15 | 14.4 |
| 15187 | 2014-02-11 | 75.0 |

## 2 OBSERVATIONS, DATA REDUCTION, AND DATA ANALYSIS

Abell 2319 was observed twice using the *Chandra* ACIS-I detectors (ObsIDs 3231 and 15187). We reprocessed the archival level 1 event lists produced by the *Chandra* pipeline in the standard manner[1] using the CIAO software package (version 4.12) and the CALDB (version 4.9.2.1) to apply the appropriate gain maps and the latest calibration products. We removed flares from light curves using the `deflare` tool with the standard time binning method recommended in the CIAO official analysis guides. Blank-sky background files provided by the *Chandra* team were extracted using the `blanksky` tool and were processed in a similar manner. The net exposure times of each observation after screening are summarized in Table 1. The resulting total net exposure time is $\sim$90 ks.

We created the count image and the exposure map, and the background image using the `fluximage` and `blanksky_image` tool, respectively. We combined all the images of both ObsIDs appropriately to create the exposure and vignetting corrected, background subtracted image (flat-fielded image). The resulting image is shown in Fig. 1. We identified point sources using the `wavdetect` tool with the scales of 1, 2, 4, 8, 16 pixels and removed them in the subsequent analysis.

We also created the thermodynamic maps. We used the contour binning algorithm (Sanders 2006) to divide the field of view into subregions used for spectral fitting. The signal-to-noise ratio of each bin is set to 100, corresponding to $\sim$10000 counts/bin. We fitted the spectrum of each region using the `phabs*apec` model with the redshift and Fe abundance fixed to 0.0557 and 0.3 solar, respectively, and the hydrogen column density set to $8\times10^{20}$ cm$^{-2}$, determined by the LAB (Leiden/Argentine/Bonn) radio HI survey (Kalberla et al. 2005). Using the best-fit temperature kT and normalization $\epsilon$, we calculated the pseudo-pressure $\tilde{p} = kT\sqrt{\epsilon/A}$ and pseudo-entropy $\tilde{s} = kT(\epsilon/A)^{-1/3}$ where $A$ is the area of the corresponding region measured in the unit of pixels. The resulting thermodynamic maps are shown in Fig. 2.

### 2.1 Surface brightness profiles of the main cold front

We extracted surface brightness profiles across the cold front with opening angles of 15° and 5°. The directions from which the 15° surface brightness profiles are extracted are indicated by the white solid partial annuli shown in Fig. 1. The center is determined at (RA, Dec)=(19:21:10.2,+43:55:46.1) so that the radial directions are perpendicular to the interface.

We modelled the observed profiles by assuming that the surface brightness is proportional to the square of a spherically symmetric density profile integrated along the line-of-sight. We used the

[1] CIAO 4.12 Homepage, Data Preparation; http://cxc.harvard.edu/ciao/threads/data.html

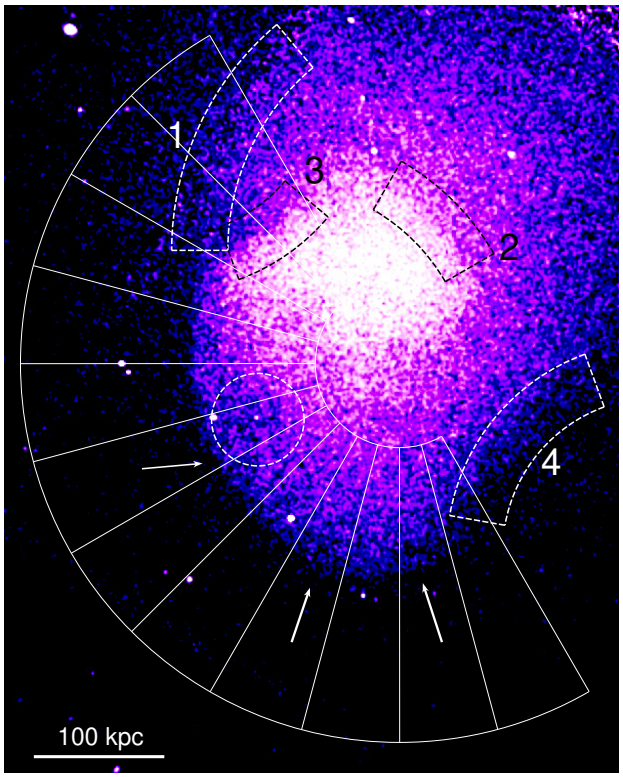


**Figure 1.** Exposure and vignetting corrected, background subtracted *Chandra* image (0.5–7.0 keV) of Abell 2319, Gaussian smoothed with $\sigma = 2$ pixel. The overlaid partial annuli shown with a solid line cover the azimuthal range of the main cold front, and are the regions from which the 15° surface brightness profiles are extracted (see also Section 2.1). The radius of the cold front abruptly decreases/increases around the directions indicated by the left/middle white arrows. The right white arrow points the surface brightness 'finger'. The numbered dashed partial annuli correspond to other interesting features. The white dashed circle denotes the surface-brightness depression. See Section 3.1 for details.

underlying radial density profile of a broken power law with a normalization jump of $j_{12}$ at the cold front radius $r_{12}$;

$$n(r) = \begin{cases} j_{12} n_0 \left(\dfrac{r}{r_{12}}\right)^{-\alpha_1} & (r \le r_{12}) \\ n_0 \left(\dfrac{r}{r_{12}}\right)^{-\alpha_2} & (r_{12} < r) \end{cases}, \quad (1)$$

where $n_0$ is the overall normalization, and $\alpha_1$ and $\alpha_2$ are the power-law slopes of the density profile inside and outside the interface.

In the fitting, we defined the likelihood function to be half of the chi-square function, corresponding to the 'exponential-term' of log-Gaussian, and performed maximum-likelihood fitting of the model to the observed data using the emcee Markov chain Monte Carlo (MCMC) package (Foreman-Mackey et al. 2013). The error bars are quoted based on the 16th and 84th percentiles of the samples in the marginalized distributions. Fig. 4 shows the azimuthal variations of the best-fit parameters. The black/grey and the red/magenta points represent the best-fit parameters for the 15° and 5° profiles, respectively.

## 3 RESULTS

### 3.1 Morphological features

In Fig. 1, there is a clear brightness edge in the southeastern direction. The thermodynamic maps shown in Fig. 2 indicate that the temperature and entropy increase abruptly across the interface from the brighter to the fainter sides, while the pressure shows a continuous change. These behaviours are typical of cold fronts and consistent with the cold front observations in the literature (e.g. Markevitch & Vikhlinin 2007).

The interface is relatively smooth but shows non-monotonicity in radius. For example, the radius is locally smaller compared to neighboring azimuths around the direction indicated by the left white arrow in Fig. 1, and increases locally around the middle white arrow. We also see a bright 'finger' of cool bright gas extending towards the west from the southernmost edge of the interface denoted by the right white arrow. It is located right at the azimuth where the cold front outline bends (the intersection of the main cold front and the edge *4*). Inside the interface, we see a local depression in surface brightness as denoted by the white dashed circle. Some of these features have been pointed out also by Wang (2019).

In addition to the main cold front, we found several other brightness features that have not been explicitly discussed in the literature; (i) we found that the main cold front diverges at its northern end. One of the branches extends further in the northern direction (marked as *1* in Fig. 1), while the other bends towards the core direction (marked as *3* in Fig. 1). (ii) we found another brightness edge to northwest from the brightness peak (marked as *2* in Fig. 1). The main coldfront, the edge *3* and the edge *2* seem to be aligned on the same spiral in this order. The edge *3* seems to be rather concave than convex. (iii) we found another concave brightness edge to southwest from the core (marked as *4* in Fig. 1). As shown in Fig. 2, either the temperature (*2*, *3* and *4*) or the entropy (*1*, *2* and *4*) seem to exhibit abrupt changes at the interface, suggesting that all of the brightness features are cold fronts.

### 3.2 Azimuthal variation of the cold front

As shown in Fig. 4, all the density profile parameters of the main cold front show significant azimuthal variations. The azimuthal profile of the break radii is not a monotonic function, and we can see several local maxima both in the 15° and 5° profiles around 160° – 170°, 200° and 240° – 260°. In particular, the the break radius abruptly decreases at ∼ 205° and increases at ∼ 245°, which are consistent with the morphological observation in the previous section.

The azimuthal profile of the density jump is mostly flat between 140° and 280°, but shows a weakening of the jump around 200°. The overall trend is consistent with what is shown in Walker et al. (2016), where the jump profile was computed using the Gaussian gradient magnitude filtering method. The azimuthal profiles of the density slope outside and inside the edge both show apparent fluctuations. The inner slope takes a local maximum around 200°, where the jump weakens. Towards the position angle of 285° – 300°, both the density jump and the difference in power-law slopes inside versus outside the break decrease.

### 3.3 Modelling of the brightness 'finger'

Fig. 5 shows the surface brightness profile extracted in the direction across the 'finger' feature. There is a coherent surface brightness excess with respect to the baseline model (magenta curve) around

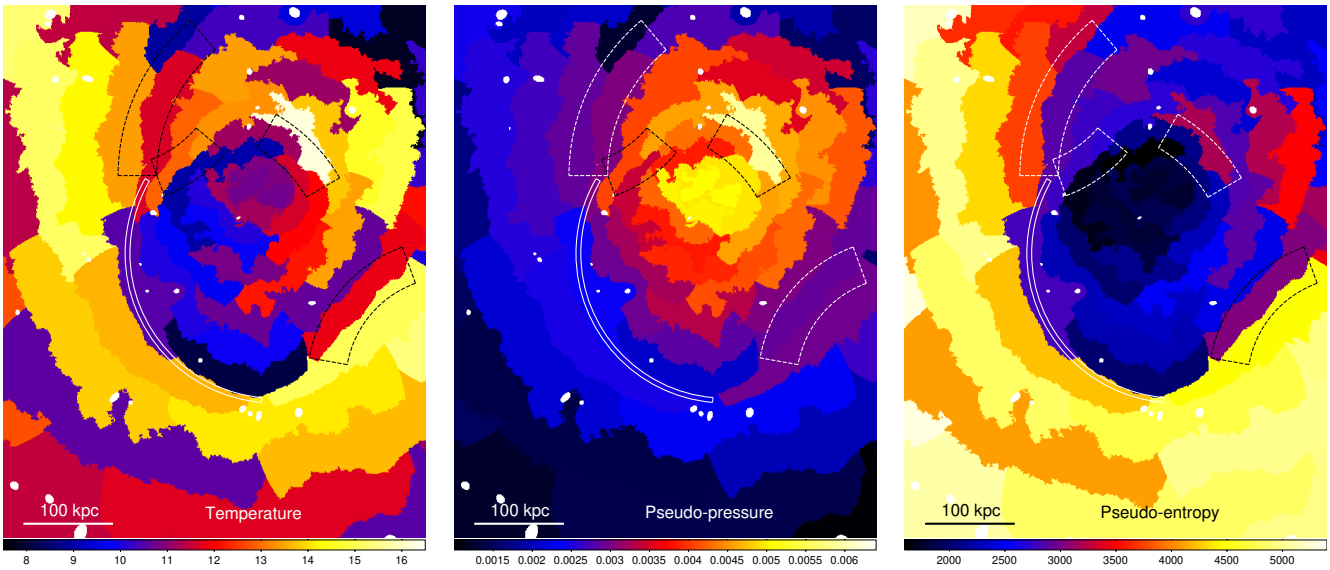


**Figure 2.** Projected thermodynamic maps. *Left:* projected temperature map in units of keV. *Middle:* pseudo-pressure map. *Right:* pseudo-entropy map. The position of the cold front is marked by the thin solid white partial annuli. The positions of other features are indicated by the dotted partial annuli (see also Fig. 1). The white circles/ellipses are the positions of point sources which are identified using the `wavdetect` tool.

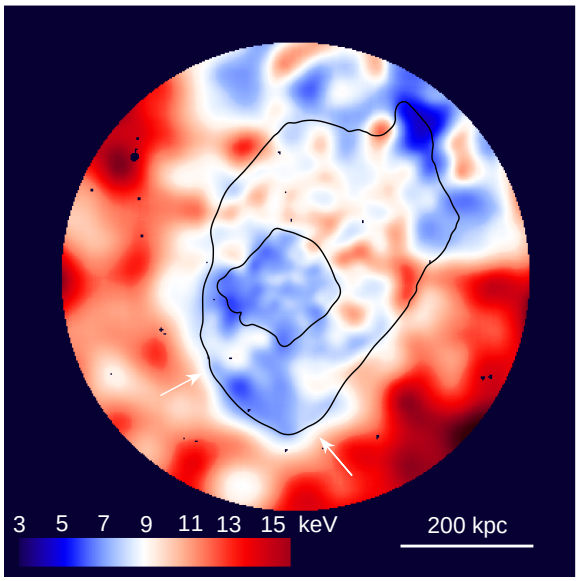


**Figure 3.** *Chandra* projected gas temperature map derived using a different method (reproduced from Wang 2019). Black contours show X-ray surface brightness (the outer contour is at the cold front). Arrow on left points to a hot spot inside the front (a circle in Fig. 1; discussed in Sec. 4.4). Arrow on right points to the region of apparent KH instabilities including the 'finger', discussed in Sec. 4.1.

$r$ = 140 arcsec, corresponding to the location of the 'finger' in the image (Fig. 1).

In order to check if this is real, we added a Gaussian component that phenomenologically represents the 'finger' to our baseline model described in Section 2.1, and fit the surface brightness profile using this model. The red curve in Fig. 5 shows the best-fitting surface brightness model with the 'finger' feature. The fit around the feature is apparently improved, with the improvement of the fit at the significance level of 4.1$\sigma$ according to the likelihood-ratio test ($-2\Delta \ln L$ = 23.3 for 3 degrees of freedom (dof))[2]. The reduced chi-square values with respect to the best-fit models are $\chi^2$/dof=122.1/101 and 98.8/98 without and with the Gaussian component, respectively.

### 3.4 Modelling of other features

Fig. 6 shows the profiles extracted in the directions marked as *1*, *2*, *3*, and *4* in Fig. 1, on which the respective best-fit baseline models are plotted. The centers are chosen to be at (RA, Dec)=(19:21:05.8,+43:57:06.7), (19:21:18.4,+43:55:34.3), (19:21:25.6,+43:59:06.8) and (19:20:53.2,+43:53:31.6), for the directions *1*, *2*, *3*, and *4*, respectively. We also modelled the profile using a model without break (simple power-law), and found that all the profiles prefer the model including the break with high significance ($-2\Delta \ln L$=81.1, 61.4, 146.0, and 264.0 for 3 degrees of freedom, for the directions *1*, *2*, *3*, and *4*, respectively). The broken power-law density model describes all the profiles well ($\chi^2$/dof=108.9/96, 43.9/36, 32.0/31, and 75.4/71 for the directions *1*, *2*, *3*, and *4*, respectively).

## 4 DISCUSSION

### 4.1 Kelvin-Helmholtz instability

As we discussed in Section 3.3, the radii of the interface fluctuate with position angle. As the azimuthal profile of the break radius has multiple minima/maxima, we can deduce that the fluctuation scale is smaller than the opening angle of the entire cold front. The emergence of sub-opening-angle scale variation of the break radii is routinely seen in numerical simulations of sloshing cold fronts where KHIs develop because of gas shear (e.g., Roediger et al. 2013b). Observationally, the existence of the sub-opening-angle scale

[2] Assuming that the number of azimuths of 12 corresponds to the number of independent random trial, the statistical significance decreases to ~3.3$\sigma$ by the look-elsewhere effect.

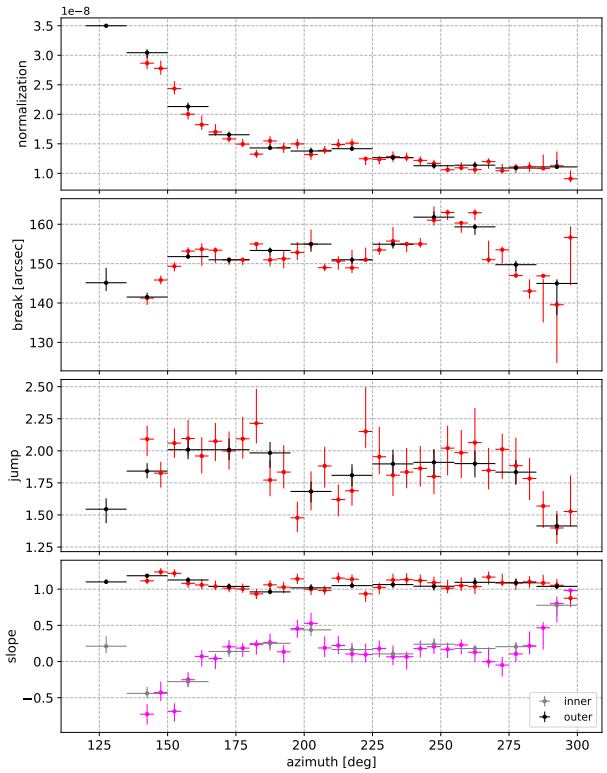


**Figure 4.** The azimuthal variations of the best-fit parameters of the broken-power-law density models (Eq. 1). *Top row:* the normalization $n_0$. *Second row:* the cold front radius $r_{12}$. *Third row:* the density jump $j_{12}$ at the cold front. *Bottom row:* the power-law slope inside (inner)/outside (outer) the break ($\alpha_1$ and $\alpha_2$). The black/grey and the red/magenta points represent the best-fit parameters for the 15° and 5° profiles, respectively.

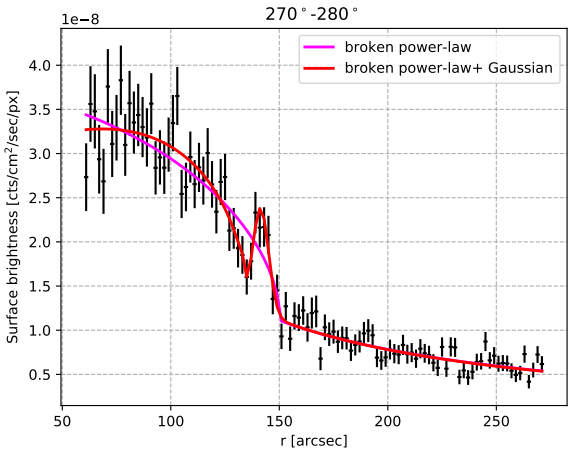


**Figure 5.** Surface brightness profile extracted in the direction across the 'finger' feature. The magenta curve is the best-fitting model using the baseline model described in Section 2.1. The red curve is the best-fitting model in which the 'finger' feature is accounted for as a Gaussian component.

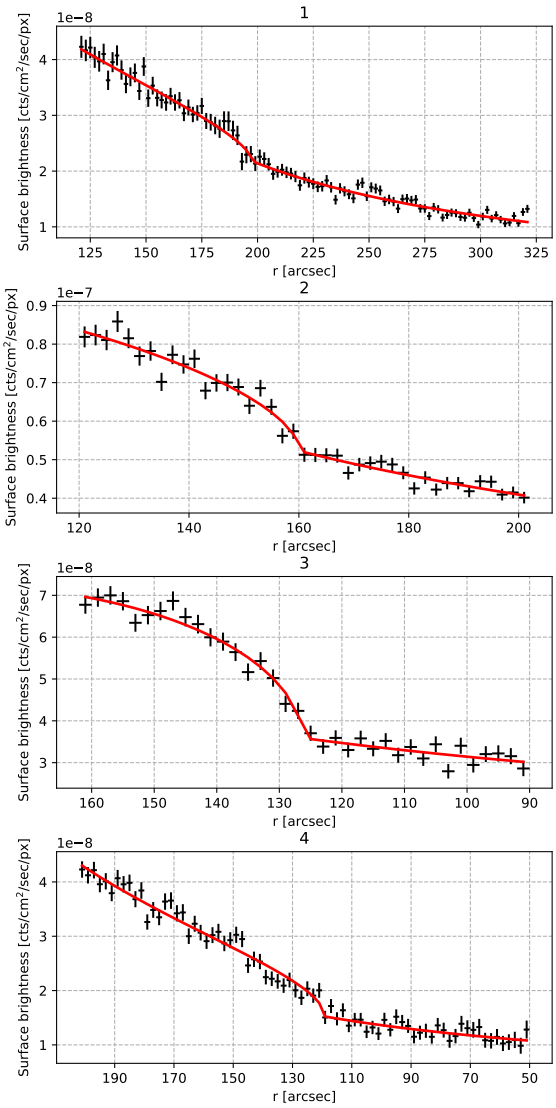


**Figure 6.** Surface brightness profiles extracted in the direction marked as *1*, *2*, *3*, and *4* in Fig. 1 from top to bottom. The red curves are the best-fit baseline model described in Section 2.1.

variation due to developing KHIs has also been indicated in the cold front in Abell 3667 by Ichinohe et al. (2017).

In addition to the cold front fluctuations, we also found a 'finger' feature at the position angle of 270° – 280° with moderate significance. The location of the 'finger' is right at the intersection of the edge *4* and the main cold front, where the cold front outline bends. This feature is morphologically similar to well-developed Kelvin-Helmholtz instabilities seen in numerical simulations (ZuHone et al. 2011; Roediger et al. 2013b). It has been shown by numerical simulations and observations that a multiple-edge structure of the surface brightness profile appears when developing KHIs exist (Roediger et al. 2013b; Su et al. 2017; Ichinohe et al. 2017, 2019) because of the KHI eddies seen in projection. As shown in Fig. 5, we see the coherent increase in surface brightness instead of multiple edges. We suggest that this is also a projected KHI eddy, detached from the main cold front due to the bend of the cold front outline. Therefore, we think that this 'finger' feature is naturally explainable with the inter-

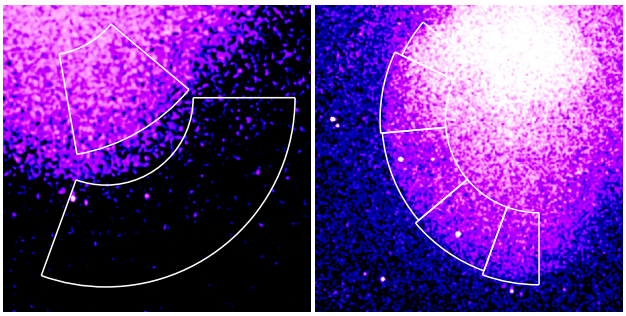

**Figure 7.** *Left:* Same as Fig. 1, close-up on the KHI candidate. The color bar is changed to visually emphasize the 'finger' feature. The overlaid regions are used for spectral analysis in Section 4.1. *Right:* Same as Fig. 1. The overlaid regions are used for spectral analysis in Section 4.4.

pretation that it is a developed KHI eddy. Note that the stripped tail of a member galaxy might be another interpretation of the 'finger', but no galaxies are found in the NASA/IPAC Extragalactic Database (NED)[3] at the corresponding location.

#### *4.1.1 Upper limit of the ICM effective viscosity*

Based on the existence (or absence) of KHI, we can derive implications on ICM microphysics. When there is a shear flow between two fluid components, KHIs start to develop. If the gas is inviscid and incompressible, all the scales show exponential development. However, finite viscosity suppresses the development of instabilities whose length scale $\lambda$ is below a certain critical value. This condition can be expressed using the critical Reynolds number $\mathrm{Re}_{\mathrm{crit}}$;

$$\mathrm{Re} = \frac{\rho \lambda V}{\mu} < \mathrm{Re}_{\mathrm{crit}} \sim a\sqrt{\Delta}, \tag{2}$$

where $V$ is the shear strength, and $\rho$ and $\mu$ are the density and viscosity on the high-viscosity side, respectively. $\Delta$ is calculated using the densities of gas on the two sides of the interface $\rho_1$ and $\rho_2$; $\Delta = (\rho_1 + \rho_2)^2/\rho_1\rho_2$, and $a$ is a numerical coefficient around dozens (Roediger et al. 2013a; Chandrasekhar 1961).

Conversely, if the KHI of the length scale of $\lambda$ exists, it indicates that the ICM viscosity should satisfy the condition

$$\mu < \frac{\rho \lambda V}{\mathrm{Re}_{\mathrm{crit}}} \sim \frac{\rho \lambda V}{a\sqrt{\Delta}}, . \tag{3}$$

Therefore, when one observes instabilities of scale $\lambda$, one can obtain the upper limit on the ICM viscosity using the gas densities and the shear strength.

In order to estimate the gas properties, we extracted spectra from the regions shown in Fig. 7 left, where the upper left and lower right partial annuli correspond to the gas inside (Inner) and outside (Outer) the interface, respectively. Note that we deliberately avoid the KHI region because the KHI would mix the gas from both sides making the interpretation difficult. The best-fit parameters are shown in Table 2, where $L_{\mathrm{in}}$ and $L_{\mathrm{out}}$ are the line-of-sight depth of the gas contributing to the spectra extracted from the Inner and Outer regions, respectively.

These gas properties are combined with Eq. 3 to obtain the upper limit on the viscosity;

$$\begin{aligned}\mu &\lesssim \frac{\rho \lambda V}{a\sqrt{\Delta}} \\ &\sim 6300\,\mathrm{g\,cm^{-1}\,s^{-1}} \left(\frac{n_{\mathrm{out}}}{3\times10^{-3}\,\mathrm{cm^{-3}}}\right)\left(\frac{\lambda}{100\,\mathrm{kpc}}\right)\left(\frac{V}{1700\,\mathrm{km\,s^{-1}}}\right) \\ &\times \left(\frac{a}{10}\right)^{-1}\left(\frac{1/\sqrt{\Delta}}{0.4}\right),\end{aligned} \tag{4}$$

where $n_{\mathrm{out}}$ is the electron density outside the interface derived in Ghirardini et al. (2018). The choices of the rather conservative fiducial values in deriving Eq. 4 are explained below.

(i) $\lambda$ is the scale of the KHI. Based on the 'eroded front' scenario discussed in detail in Section 4.3.1, assuming that the pitch of the *feathery* structures represents the wavelength of the scale that can grow, $\lambda \sim 100$ kpc can be inferred. The temperature map in Fig. 3 exhibits multiple eddy-like structures of cool gas at the 'eroded' region and the pitch of the cool gas components is similarly about 100 kpc. The current data quality precludes the structures of smaller scales from being detected and it is possible that the existing scales may even be smaller, but in any case, ~100 kpc seems to be a reasonable choice for the conservative estimation of $\lambda$. (ii) $V$ is the relative shear velocity of the gases on two sides of the front. Since gas sloshing is subsonic, the Mach number of the shear is expected to be well below the sound speed (Markevitch et al. 2001; Wang & Markevitch 2018). As we do not observe shock features in the image, we simply adopted the current fiducial value of $V \sim 1700\,\mathrm{km\,s^{-1}}$, the sound speed for the cooler side temperature (10.2 keV, see Table 2). (iii) $a$ is the numerical coefficient and several estimations ($a \sim 10$, 16 and 64) are presented by Roediger et al. (2013a). The most conservative choice is $a = 10$ and we took this value. Note that it is pointed out in Ichinohe et al. (2017) that the values 10 and 16 may be too conservative because some simulations with the Reynolds number above these values show the suppression of instabilities (e.g., Fig. 8 in Roediger et al. 2015). (iv) The $1/\sqrt{\Delta}$ factor in Eq. 3 depends weakly on the actual geometry and takes a value around ~0.4 for $L_{\mathrm{out}}/L_{\mathrm{in}} = 1-10$.

The isotropic, temperature-dependent Spitzer viscosity is

$$\mu_{\mathrm{Sp}} = 21000\,\mathrm{g\,cm^{-1}\,s^{-1}}\left(\frac{kT}{14.7\,\mathrm{keV}}\right)^{5/2}, \tag{5}$$

where the Coulomb logarithm $\ln\Lambda = 40$ is assumed (Spitzer 1965; Sarazin 1986; Roediger et al. 2013b). We can safely reach the conclusion that the ICM viscosity is suppressed by at least factor 3 below the full Spitzer value.

Recently, several attempts have been made to infer the ICM viscosity by this methodology. Using the merger cold front in Abell 3667, Ichinohe et al. (2017) estimated the upper limit of the ICM effective viscosity to be $\mu \lesssim 200\,\mathrm{g\,cm^{-1}\,s^{-1}}$. Similarly, using the merger cold front in NGC 1404 in the Fornax cluster, (Su et al. 2017) put an upper limit at 5% of the Spitzer value.

The estimation of the upper limit of the ICM viscosity using sloshing cold fronts (especially sloshing in the plane of the sky) has been difficult due to the difficulty of estimating the shear velocity perpendicular to the line-of-sight direction. Estimates based on the comparison of the observation to the tailored simulation have been made (Roediger et al. 2013b; Werner et al. 2016a). Using the sloshing cold front in Abell 2142, which exhibits multiple KH eddies, and the gas velocity estimate based on centripetal acceleration, Wang & Markevitch (2018) derived the first quantitative upper limit, $\mu < 1/5\,\mu_{\mathrm{Sp}}$.

Our result is consistent with the picure presented in the literature

[3] The NASA/IPAC Extragalactic Database (NED) is funded by the National Aeronautics and Space Administration and operated by the California Institute of Technology.

**Table 2.** Best-fitting thermodynamic parameters for the region shown in Fig. 7.

| Region | Temperature (keV) | Fe abundance (solar) | Electron density ($10^{-3}$cm$^{-3}$) |
|---|---|---|---|
| Inner | 10.2±0.5 | 0.62±0.14 | $8.7 \pm 0.1 \times (L_{\rm in}/100\,{\rm kpc})^{-1/2}$ |
| Outer | 14.7±1.3 | $0.59^{+0.24}_{-0.22}$ | $4.9 \pm 0.1 \times (L_{\rm out}/100\,{\rm kpc})^{-1/2}$ |

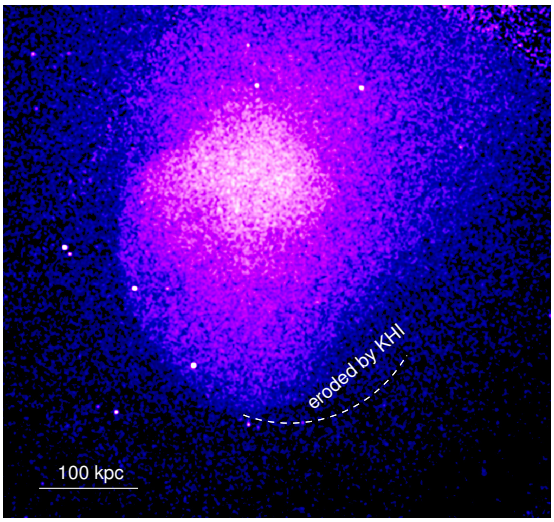


**Figure 8.** A possible origin of the southwest concave feature is KHI developing at this position of the cold front and destroying the sharp contact discontinuity (which otherwise would continue as schematically shown by dashed line).

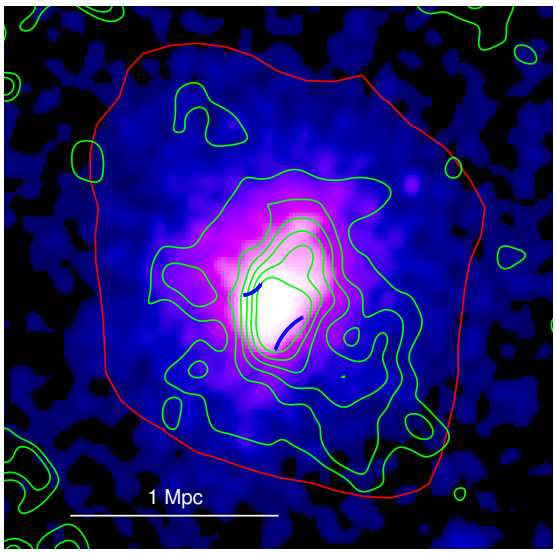


**Figure 9.** A wider-field archival *ROSAT* PSPC image of Abell 2319 (0.5–2 keV), with two concave segments of the cold front seen by *Chandra* (the edges *3* and *4* in Fig. 1) marked by blue arcs near the center. Contours overlay diffuse radio emission at 1.4 GHz from *VLA* (green) and *GBT* (red), reproduced from Storm et al. (2015).

that the ICM viscosity is suppressed from the full Spitzer viscosity. The reason that we were able to derive a meaningful upper limit using very conservative parameters, is the high temperature ($\gtrsim$10 keV) of the system. We used the sound speed, which depends on the square-root of the temperature, for the shear velocity $V$ (Eq. 3), while the full Spitzer viscosity is proportional to $kT^{5/2}$ (Eq. 5). The viscosity suppression fraction is proportional to the inverse of the temperature squared; $\mu/\mu_{\rm sp} \propto kT^{-2}$, and therefore higher temperature systems are more advantageous.

### 4.2 Split of the main cold front

As shown in Fig. 1, the northern end of the main cold front appears to split in two – one extends rather along the way of the main cold front (marked as *1*), and the other bends sharply to inside the interface (marked as *3*). A similar split of the cold front is found at ~730 kpc from the Perseus cluster core (Walker et al. 2018). Several observational/simulation studies have suggested the existence of such a double-layered structure of cold fronts due to KHIs developing along sloshing cold fronts (e.g., Roediger et al. 2013b; Ichinohe et al. 2019). If one thinks of the cold front as a 3D surface, this double edge may be a projection of an inward depression in the front surface created by KHI. We will also discuss a more exotic possibility below.

### 4.3 Southwest concave discontinuity

Southwest of the center, the main cold front continues as an interesting, much less sharp, concave surface brightness discontinuity (the edge *4* in Fig. 1). Below we discuss two possible scenarios for it.

#### 4.3.1 *Erosion of the front by KHI*

One possible cause of this feature is the gas dynamics related to core sloshing, similar to the interpretation suggested by Werner et al. (2016b) for a concave discontinuity in the Ophiuchus cluster. Hydrodynamic simulations suggest that such deformations of the cold front shape can arise during core sloshing (see e.g., Fig. 22 in Ascasibar & Markevitch 2006). The gas flow tangential to the front surface should result in KHIs, which at some locations should grow fast enough to disrupt the discontinuity entirely. The southwest concave structure may be such a region of the front eroded by KHI, as schematically depicted in Fig. 8. Although the surface brightness profile (Fig. 6 bottom) and the thermodynamic maps (Fig. 2) both indicate that the gas properties are different inside and outside this edge, neither the profile nor the image (Fig. 1) show sharp features. A close inspection of the X-ray image shows wavy *feathery* structure of the discontinuity, similar to the Perseus cluster cold front (Ichinohe et al. 2019). The 'finger' discussed in Section 4.1 is the most prominent of those *feathers*. This region may have large KH rolls mixing the gases on two sides of the former discontinuity. In projection, they may not appear as the typical simulated KHI rolls (e.g., Roediger et al. 2013b) because of their more complex 3D structure.

#### 4.3.2 *A giant AGN outburst?*

We also consider an interesting, but at this point rather speculative alternative possibility. A similar concave X-ray feature near the core of the Ophiuchus cluster, upon comparison with the radio data, turned

out to be the result of the most powerful known AGN explosion (Giacintucci et al. 2020). AGN outbursts generate powerful jets that transport large amounts of energy from the nucleus and deposit it at a distance, typically within the cluster cool core. This process creates a pair of bubbles in the ICM, filled with relativistic particles mixed with hot ICM. In the X-ray images, these bubbles are seen as symmetric pairs of round cavities or depressions; typical examples are the Perseus cluster (Fabian et al. 2006), Hydra A (Nulsen et al. 2005) and MS0735+74 (McNamara et al. 2005). Apparently, the outburst can be powerful enough for these bubbles to form outside the cool core, as in the Ophiuchus cluster (Giacintucci et al. 2020). In such a case, the X-ray cavity can be difficult to see in its entirety — only its innermost segment, closest to the core, may be seen as a concave feature. However, the pair of diffuse radio lobes filling the cavity should always be present — though, as in Ophiuchus, they may emit at very low radio frequencies.

In Fig. 9, we show a wider-field archival X-ray image of Abell 2319 from *ROSAT* PSPC, with overlays of 1.4 GHz radio maps from *VLA* and *GBT*, reproduced from Storm et al. (2015). For *VLA*, compact sources have been removed to the degree possible. For *GBT*, only the lowest contour is shown. The *GBT* angular resolution is low, comparable to the size of the cluster cool core, but it does not miss the faint extended emission on large angular scales, because it is a full-aperture instrument. The radio emission consists of a relatively bright minihalo that fills the cluster cool core and follows the distribution of the cool gas, and a more extended emission, which Storm et al. (2015) interpret as a giant radio halo enveloping the minihalo (for review of the types of diffuse radio sources in clusters see van Weeren et al. (2019)). A similar observation was made by Govoni et al. (2004) using less sensitive *WSRT* radio data and earlier *Chandra* data.

Interestingly, the *GBT* image reveals a faint radio extension to the NE, opposite to the SW extension seen by the *VLA* (it may have been missed by the *VLA* because of the limitations of an interferometer). Fig. 9 also marks the two concave X-ray features that we find on the opposite sides of the cluster core. It is conceivable that those features are the inner boundaries of two giant X-ray cavities, and the radio emission that extends beyond the minihalo is in fact a pair of giant radio lobes that fill those cavities, similar to the Ophiuchus lobe. Of course, a higher-resolution radio map, sensitive to the large-scale emission and preferably obtained at low radio frequencies (where the aged AGN radio lobes should be relatively brighter), is required to determine whether this is a pair of radio lobes and not a giant halo. *LOFAR* may be able to derive such a map. Recently, *LOFAR* has resolved a presumed 'giant halo' in another cluster, Abell 2390, into a pair of giant radio lobes (Savini et al. 2019) coincident with X-ray cavities (Vikhlinin et al. 2005).

While this scenario is speculative without better radio data, it is interesting to estimate the energy of an AGN outburst that would be required to create these putative bubbles. The radius of curvature of the edge *4* is ∼130 kpc. Using the density and temperature profiles shown in Ghirardini et al. (2018), the total cavity enthalpy (Churazov et al. 2002; Bîrzan et al. 2004) is estimated at $\sim 5\times10^{61}$ erg. This is comparable with the most powerful cluster AGN outbursts reported in the literature (McNamara et al. 2005; Vantyghem et al. 2014; Werner et al. 2016b; Giacintucci et al. 2020). Such energy would be more than sufficient to completely disrupt a cool core (we note here that A2319 does not have a classic cool core, even though it does have a cD galaxy). If this scenario is supported by future radio data, it may indicate that such powerful outbursts are more common than we thought.

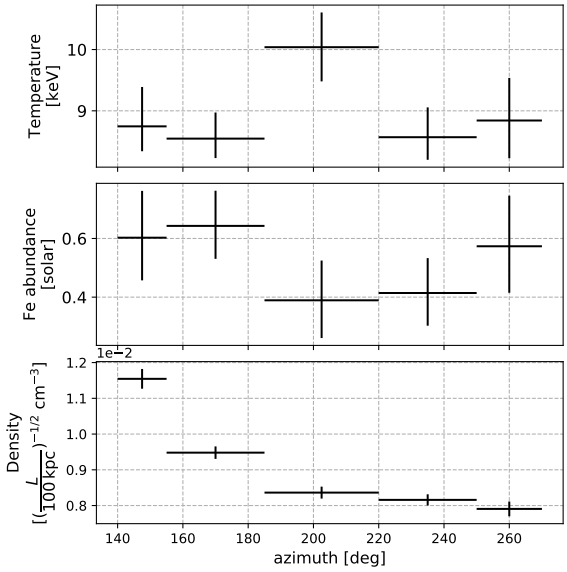


**Figure 10.** The azimuthal variations of the thermodynamic properties inside the cold front.

### 4.4 A hole in the front

As we noted in Section. 3.2, the amplitude of the gas density jump at the front shows a local drop around the position angle of 200°, where the azimuthal profile of the inner power-law slope takes a local maximum (Fig. 4). A close examination of the X-ray image shows a curious depression in the X-ray brightness inside the cold front (dashed circle in Fig. 1). The gas temperature at this position is higher than elsewhere inside the cold front, see Fig. 3, where this spot is marked by an arrow. We fit spectra in several regions inside the front shown in Fig. 7 right (the outer radii of the sectors are determined by averaging the best-fit break radii shown in Fig. 4). The fit results are given in Fig. 10. To obtain the electron number density, we assumed the line-of-sight depth of the X-ray emitting gas is $L$ =100 kpc. The fits confirm the higher ICM temperature at the position of the brightness depression. We offer two explanations for this feature.

#### *4.4.1 Non-uniform gas mixing*

In one, the higher-entropy gas in this spot (Fig. 2 right) originates outside the front. It could be transported under the front, for example, as a result of the KH instability (e.g., Roediger et al. 2013a). It is conceivable that this may happen in 3D without disrupting the sharp front boundary that we see in projection. It is expected that both the density contrast and the difference of the density slopes are smeared due to the gas mixing. The KHI-induced gas mixing is more efficient around the position angle of 200° than the surrounding angles, i.e. a KHI eddy may 'funnel' hotter gas from the outside of the front that penetrates below the cold front interface at this location.

#### *4.4.2 A breach in magnetic insulation layer?*

Another interesting possibility is heat conduction from the outer side of the front. In general, the gas inside a cold front should be thermally insulated from the outer gas by a magnetic field layer parallel to the front surface, which should form as a result of magnetic draping

(Markevitch & Vikhlinin 2007). In the ICM, the heat is not transmitted across the magnetic field lines. However, MHD simulations by ZuHone et al. (2013) showed that such insulation is not perfect — some field lines can cross from the inner to the outer region. Because sloshing cold fronts have a finite 'height' in the direction perpendicular to the plane of the sloshing spiral, some field lines may climb over the front 'fence.' Other lines can pass through the front because of imperfect field draping. Thermal conduction along such stray magnetic field lines may heat the gas locally inside the front and produce high-entropy regions such as the one we observe.

## 5 CONCLUSIONS

In this paper, we studied the cold front in Abell 2319 in detail using ~90 ks archival *Chandra* data. The main results of our work are summarized below.

(i) We find several substructures associated with the cold front, including the sub-opening-angle scale variation of the interface radii of the cold front and the 'finger' of cool bright gas extending outwards from the front. These features are naturally explainable by Kelvin-Helmholtz instabilities developing on the interface.

(ii) Thanks to the high temperature of the system, based on this interpretation, we can place an upper limit on the ICM viscosity at several times below the full isotropic Spitzer viscosity, with rather conservative assumptions about the geometry and shear velocity.

(iii) We found that the northern edge of the main cold front diverges into two different directions.

(iv) We found a concave surface brightness discontinuity southwest of the cluster core. This can result either from merger induced gas dynamics or from one of the most powerful $\sim 5 \times 10^{61}$ erg, AGN outbursts.

(v) We found a hotter region inside the cold front. The density jump and the difference of density slopes between the gas inside and outside the interface are weaker at the corresponding azimuths. We suggest that this may be due either to non-uniform gas mixing or a hole in the magnetic layer that thermally insulates the front.

## ACKNOWLEDGEMENTS

YI is supported by the Grants-in-Aid for Scientific Research by the Japan Society for the Promotion of Science with KAKENHI grant Nos. JP18H05458, JP20K14524 and JP20K20527. A. Simionescu is supported by the Women In Science Excel (WISE) programme of the Netherlands Organisation for Scientific Research (NWO), and acknowledges the World Premier Research Center Initiative (WPI) and the Kavli IPMU for the continued hospitality. SRON Netherlands Institute for Space Research is supported financially by NWO. NW is supported by the MUNI Award for Science and Humanities funded by the Grant Agency of Masaryk University.

## DATA AVAILABILITY

The data underlying this article will be shared on reasonable request to the corresponding author.

## REFERENCES

Ascasibar Y., Markevitch M., 2006, ApJ, 650, 102
Bîrzan L., Rafferty D. A., McNamara B. R., Wise M. W., Nulsen P. E. J., 2004, ApJ, 607, 800
Chandrasekhar S., 1961, Hydrodynamic and hydromagnetic stability. Oxford University Press
Churazov E., Sunyaev R., Forman W., Böhringer H., 2002, MNRAS, 332, 729
Eckert D., et al., 2014, A&A, 570, A119
Edge A. C., Stewart G. C., Fabian A. C., Arnaud K. A., 1990, MNRAS, 245, 559
Fabian A. C., Sanders J. S., Taylor G. B., Allen S. W., Crawford C. S., Johnstone R. M., Iwasawa K., 2006, MNRAS, 366, 417
Farnsworth D., Rudnick L., Brown S., Brunetti G., 2013, ApJ, 779, 189
Feretti L., Giovannini G., Böhringer H., 1997, New Astron., 2, 501
Foreman-Mackey D., Hogg D. W., Lang D., Goodman J., 2013, PASP, 125, 306
Ghirardini V., Ettori S., Eckert D., Molendi S., Gastaldello F., Pointecouteau E., Hurier G., Bourdin H., 2018, A&A, 614, A7
Ghizzardi S., Rossetti M., Molendi S., 2010, A&A, 516, A32
Giacintucci S., Markevitch M., Johnston-Hollitt M., Wik D. R., Wang Q. H. S., Clarke T. E., 2020, ApJ, 891, 1
Govoni F., Enßlin T. A., Feretti L., Giovannini G., 2001, A&A, 369, 441
Govoni F., Markevitch M., Vikhlinin A., van Speybroeck L., Feretti L., Giovannini G., 2004, ApJ, 605, 695
Harris D. E., Miley G. K., 1978, A&AS, 34, 117
Hurier G., Adam R., Keshet U., 2019, A&A, 622, A136
Ichinohe Y., Werner N., Simionescu A., Allen S. W., Canning R. E. A., Ehlert S., Mernier F., Takahashi T., 2015, Monthly Notices of the Royal Astronomical Society, 448, 2971
Ichinohe Y., Simionescu A., Werner N., Takahashi T., 2017, MNRAS, 467, 3662
Ichinohe Y., Simionescu A., Werner N., Fabian A. C., Takahashi T., 2019, MNRAS, 483, 1744
Kalberla P. M. W., Burton W. B., Hartmann D., Arnal E. M., Bajaja E., Morras R., Pöppel W. G. L., 2005, A&A, 440, 775
Lodders K., Palme H., 2009, Meteoritics and Planetary Science Supplement, 72, 5154
Machacek M., Jones C., Forman W. R., Nulsen P., 2006, ApJ, 644, 155
Markevitch M., 1996, ApJ, 465, L1
Markevitch M., Vikhlinin A., 2007, Phys. Rep., 443, 1
Markevitch M., et al., 2000, ApJ, 541, 542
Markevitch M., Vikhlinin A., Mazzotta P., 2001, ApJ, 562, L153
McNamara B. R., Nulsen P. E. J., Wise M. W., Rafferty D. A., Carilli C., Sarazin C. L., Blanton E. L., 2005, Nature, 433, 45
Million E. T., Allen S. W., 2009, MNRAS, 399, 1307
Nulsen P. E. J., McNamara B. R., Wise M. W., David L. P., 2005, ApJ, 628, 629
O'Hara T. B., Mohr J. J., Guerrero M. A., 2004, ApJ, 604, 604
Owers M. S., Nulsen P. E. J., Couch W. J., Markevitch M., 2009, ApJ, 704, 1349
Planck Collaboration et al., 2016, A&A, 594, A27
Roediger E., Kraft R. P., Nulsen P., Churazov E., Forman W., Brüggen M., Kokotanekova R., 2013a, MNRAS, 436, 1721
Roediger E., Kraft R. P., Forman W. R., Nulsen P. E. J., Churazov E., 2013b, ApJ, 764, 60
Roediger E., et al., 2015, ApJ, 806, 104
Sanders J. S., 2006, MNRAS, 371, 829
Sarazin C. L., 1986, Reviews of Modern Physics, 58, 1
Savini F., et al., 2019, A&A, 622, A24
Spitzer L., 1965, Physics of fully ionized gases. New York: Interscience Publication
Storm E., Jeltema T. E., Rudnick L., 2015, MNRAS, 448, 2495
Su Y., et al., 2017, ApJ, 834, 74
Sugawara C., Takizawa M., Nakazawa K., 2009, PASJ, 61, 1293
Sunyaev R. A., Zeldovich Y. B., 1972, Comments on Astrophysics and Space Physics, 4, 173
Ueda S., Ichinohe Y., Molnar S. M., Umetsu K., Kitayama T., 2020, ApJ, 892, 100

Vantyghem A. N., McNamara B. R., Russell H. R., Main R. A., Nulsen P. E. J., Wise M. W., Hoekstra H., Gitti M., 2014, MNRAS, 442, 3192
Vikhlinin A., Markevitch M., Murray S. S., 2001a, ApJ, 549, L47
Vikhlinin A., Markevitch M., Murray S. S., 2001b, ApJ, 551, 160
Vikhlinin A., Markevitch M., Murray S. S., Jones C., Forman W., Van Speybroeck L., 2005, ApJ, 628, 655
Walker S. A., Sanders J. S., Fabian A. C., 2016, MNRAS, 461, 684
Walker S. A., Hlavacek-Larrondo J., Gendron-Marsolais M., Fabian A. C., Intema H., Sanders J. S., Bamford J. T., van Weeren R., 2017, MNRAS, 468, 2506
Walker S. A., ZuHone J., Fabian A., Sand ers J., 2018, Nature Astronomy, 2, 292
Wang Q. H. S., 2019, PhD thesis, University of Maryland
Wang Q. H. S., Markevitch M., 2018, ApJ, 868, 45
Wang Q. H. S., Markevitch M., Giacintucci S., 2016, ApJ, 833, 99
Werner N., et al., 2016a, MNRAS, 455, 846
Werner N., et al., 2016b, MNRAS, 460, 2752
Yan P.-F., Yuan Q.-R., Zhang L., Zhou X., 2014, AJ, 147, 106
ZuHone J. A., Markevitch M., Lee D., 2011, ApJ, 743, 16
ZuHone J. A., Markevitch M., Ruszkowski M., Lee D., 2013, ApJ, 762, 69
ZuHone J. A., Kunz M. W., Markevitch M., Stone J. M., Biffi V., 2015, ApJ, 798, 90
van Weeren R. J., de Gasperin F., Akamatsu H., Brüggen M., Feretti L., Kang H., Stroe A., Zandanel F., 2019, Space Sci. Rev., 215, 16

This paper has been typeset from a TEX/LATEX file prepared by the author.